Computational Study of Spout Collapse and Impact of Partition Plate in a Double Slot-Rectangular Spouted Bed

Shiliang Yang
School of Chemical and Biomedical Engineering, Nanyang Technological University, Singapore 637459, Singapore

Ke Zhang
Shanghai Nuclear Engineering Research & Design Institute, Shanghai 200233, P.R. China

State Key Laboratory of Clean Energy Utilization, Zhejiang University, Hangzhou 310027, P.R. China

Jia Wei Chew
School of Chemical and Biomedical Engineering, Nanyang Technological University, Singapore 637459, Singapore

Singapore Membrane Technology Center, Nanyang Environment and Water Research Institute, Nanyang Technological University, Singapore 637141, Singapore

DOI 10.1002/aic.14973
Published online August 4, 2015 in Wiley Online Library (wileyonlinelibrary.com)

Gas-solid hydrodynamics in a three-dimensional slot-rectangular double-spouted bed was numerically investigated by a combined approach of discrete element method and computational fluid dynamics, and the knowledge gained was extended to understand the mechanisms leading to operational instability due to the collapse of a spout, along with the beneficial impact of inserting a vertical partition plate. The setup investigated has two diverging bases and contains up to 2,590,000 particles. The computational results show different behaviors of pressure drop, in terms of average value, fluctuations, and power spectral trends, in the five distinct flow regimes corresponding to various superficial gas velocities. Two types of spout shapes are observed under stable spouting conditions, and the spout sizes are quantified. When one of the spouts chokes then collapses, complex interactions between the chambers are identified. Furthermore, the insertion of a vertical partition plate between two chambers appears to be an effective way to prevent the interactions between adjacent fountains, which is advantageous for improving the operational stability of such systems upon scale-up. © 2015 American Institute of Chemical Engineers *AIChE J*, 61: 4087–4101, 2015
Keywords: multiple-spouted bed, hydrodynamics, numerical analysis, scale-up, multiphase flow

Introduction

The conventional spouted bed operated in a conical or conical-cylindrical vessel is well-acknowledged to provide for efficient gas-particle contacting,[1–4] hence is beneficial for a wide range of physical and chemical processes, such as drying of granular materials, coating of tablets, blending of solids, pyrolysis of shale, gasification, and coal combustion.[5–7] However, it is rarely used in large-scale industrial processes due to the difficulties in scale-up. Simply scaling up a single-chamber bed is not practical in the industry due to the complications related to a taller bed, including: (1) the requirement of a larger compressor to overcome the increased pressure; (2) the difficulty with maintaining a steady spout, as the spout tends to sway sideways; and (3) the higher residence time of the particles in both the spout and fountain regions, which is harmful for the particles due to, for example, overheating or overcoating. Thus, scale-up has to be done by combining multiple chambers primarily to limit the bed heights. Unfortunately, the problem with multiple chambers is that the aligned chambers exchange both gas and solid with each other, thereby giving rise to potential operational instability; the mechanism causing the instabilities has to be understood, which is the focus of the current effort. There have been some efforts toward the scale-up of multiple spouted beds with circular inlets.[8–12] Specifically, these spouted beds are designed such that multiple chambers are combined or multiple jets are arrayed at the bottom of a single chamber. Mujumdar[13] proposed the "two-dimensional (2-D) spouted bed" to overcome scaling-up difficulties of conventional spouted beds and suggested multiple spouting columns. Dogan et al.[14] and Freitas et al.[15] renamed it as "Slot-rectangular spouted bed" for they found significant three-dimensional (3-D) effects when increasing the column depth. However, only a few studies focused on investigating the multiple slot-rectangular spouted beds. Via experiments, Chen[16] investigated the hydrodynamics, stability, and scale-up of single and multiple slot-

Correspondence concerning this article should be addressed to K. Zhang at zhangke_1984r@163.com or J. W. Chew at JChew@ntu.edu.sg.

rectangular spouted beds with flat/diverging base(s), while Ren et al.[12] investigated the flow patterns and transitions in a multiple-spouted bed. Buijtenen et al.[17] took a numerical and experimental approach to understand a pseudo 2-D, flat-bottom, triple-spout fluidized bed, and the effects of multiple spouts on the bed dynamics were revealed.

Numerical simulations have been widely used to study the dense gas-solid fluidized systems in recent years. The discrete element method (DEM) coupled with computational fluid dynamics (CFD) has been proven to be a powerful tool to resolve particulate flows at the individual particle level.[18–23] Successful applications of the DEM simulations to the 2-D spouted beds and the axisymmetric spouted beds have been reported extensively in literature.[24–29]

However, most of the slot-rectangular spouted beds studied by DEM so far have been thin, and nearly all of them are single-spouted beds except Buijtenen et al.,[17] who studied a pseudo 2-D column with multiple slots. Furthermore, particle numbers in these studies varied from several thousands to several hundreds of thousands due to the need for considerable computational resource to track the solid motion in the lab-scale apparatus. Recently, Yang et al.[30] numerically investigated the gas-solid hydrodynamics and flow regime in a single slot-rectangular spouted bed using the parallel CFD-DEM coupling approach, following which the hydrodynamics and flow pattern in the double slot-rectangular spouted beds studied revealed that the minimum spouting velocity was elevated compared with a single-chamber system.[31] Furthermore, gradually decreasing the spouting velocity in these two chambers leads to the collapse of one of the spouting structures. The termination of a spout in the double spouted bed reflects the flow instability in the two chambers. However, the intrinsic mechanism behind the appearance of this special flow regime, which stems from the instantaneous gas-solid interchange between the two chambers of the system, is difficult to be experimentally monitored, which hence hampers scale-up efforts. An in-depth investigation on the spout collapse mechanism is necessary to optimize the design of internal insertions for circumventing such flow instabilities in the practical operation. The bed hydrodynamics in the system with a vertically inserted partition plate between the chambers has been studied.[32] Although the results demonstrated that the insertion of the partition plate leads to the formation of two parallel fountains without solid exchange and the elevation of pressure drop in the system, the reason why the vertically inserted partition plate can be used to improve the stability of the whole system has not been addressed. However, the detailed understanding on the effect of the partition plate on operational stability of this apparatus is extremely critical for the design and scale-up of this apparatus.

Thus, based on the previous numerical work, the objective of this study is to gain insights into the intrinsic mechanisms of the collapse of one spouting structure and the effect of the partition plate on improving the system stability in a lab-scale double slot-rectangular spouted bed by means of the CFD-DEM approach. The apparatus investigated here using the open-source MFIX_DEM codes[33–35] is based on that experimentally investigated by Chen,[16] and consists of two chambers with diverging bases and up to millions of particles. First, the pressure drop and the corresponding spectrum analysis of the bed operated in five flow regimes are presented. Then, the detailed gas-solid flow dynamics in the 3-D multiple spouted beds are discussed, after which the critical flow of the gas phase before and after the spouting collapse is examined. Finally, the effect of partition plate on improving the spouting stability is analyzed.

Numerical Methods

Governing equations of gas motion

The motion of the gas phase is governed by the equations of continuity and momentum conservation equations, and the local variables averaged over a computational cell. The gas is assumed to be incompressible, and its motion is described using the Navier–Stokes equations. For the conically spouted bed, as has been reported by Zhao et al.[36] and Ren et al.,[37] the ignorance of turbulence in this unique apparatus may lead to difficulties in the modeling of the spout-annulus interface. Thus, this aspect has been taken into account in this work and the governing equations for gas phase are presented as follows

$$\frac{\partial\left(\varepsilon_g\rho_g\right)}{\partial t}+\frac{\partial\left(\varepsilon_g\rho_g\mathbf{u}_i\right)}{\partial x_i}=0 \tag{1}$$

$$\begin{aligned}\frac{\partial}{\partial t}\left(\varepsilon_g\rho_g\mathbf{u}_i\right)+\frac{\partial\left(\varepsilon_g\rho_g\mathbf{u}_i\mathbf{u}_j\right)}{\partial x_j}&=-\varepsilon_g\frac{\partial p_g}{\partial x_i}\\ -\frac{1}{V_{\text{cell}}}\sum_{i=1}^{n}\mathbf{f}_{d,i}+\rho_g\varepsilon_g\mathbf{g}+\frac{\partial}{\partial x_j}&\left[\varepsilon_g(\mu+\mu_t)\left(\frac{\partial\mathbf{u}_j}{\partial x_i}+\frac{\partial\mathbf{u}_i}{\partial x_j}\right)\right]\end{aligned} \tag{2}$$

where ρ_g, p, μ, $\mathbf{g}$, and $\mathbf{u}$ represent the gas density, the gas pressure, the gas dynamic viscosity, gravitational acceleration, and the gas velocity in the local cell, respectively. Also, n is the total number of particles in the current cell. In addition, μ_t is the turbulent viscosity calculated from k-ε turbulent model as $\mu_t=c_\mu\rho_g k^2/\varepsilon_t$, where c_μ is a constant of 0.09, k is turbulence kinetic energy, and ε_t is the turbulence dissipation rate. Also, $\mathbf{f}_{d,i}$ is the drag force exerted on particle i located in the current cell evaluated. The voidage ε_g is calculated as

$$\varepsilon_g=1-\frac{\sum_{i=1}^{n}V_{pi}}{V_{\text{cell}}} \tag{3}$$

where V_{pi} and V_{cell} represent the volume of particle i occupied by the current cell and the volume of this cell, respectively.

The gas turbulence kinetic energy and momentum dissipation equations are expressed as follows

$$\begin{aligned}\frac{\partial}{\partial t}\left(\varepsilon_g\rho_g k\right)+\frac{\partial\left(\varepsilon_g\rho_g k\mathbf{u}_j\right)}{\partial x_j}&\\ =\frac{\partial}{\partial x_j}\left[\varepsilon_g\left(\mu+\frac{\mu_t}{\sigma_k}\right)\frac{\partial k}{\partial x_j}\right]+\varepsilon_g\mu_t\frac{\partial\mathbf{u}_i}{\partial x_j}&\left(\frac{\partial\mathbf{u}_j}{\partial x_i}+\frac{\partial\mathbf{u}_i}{\partial x_j}\right)-\varepsilon_g\rho_g\varepsilon_t\end{aligned} \tag{4}$$

$$\begin{aligned}\frac{\partial}{\partial t}\left(\varepsilon_g\rho_g\varepsilon_t\right)+\frac{\partial\left(\varepsilon_g\rho_g\varepsilon_t\mathbf{u}_j\right)}{\partial x_j}&=\frac{\partial}{\partial x_j}\left[\varepsilon_g\left(\mu+\frac{\mu_t}{\sigma_t}\right)\frac{\partial\varepsilon_t}{\partial x_j}\right]\\ +\frac{\varepsilon_g c_1\varepsilon_t}{k}\mu_t\frac{\partial\mathbf{u}_i}{\partial x_j}&\left(\frac{\partial\mathbf{u}_j}{\partial x_i}+\frac{\partial\mathbf{u}_i}{\partial x_j}\right)-\varepsilon_g c_2\rho_g\frac{\varepsilon_t^2}{k}\end{aligned} \tag{5}$$

where c_1 and c_2 are constants of 1.44 and 1.92, respectively. Moreover, σ_ε is the turbulent Prandtl number for ε_t corresponding to a value of 1.3, while σ_k is the turbulent Prandtl number for k corresponding to a value of 1.0.

Governing equations of solid motion

In the CFD-DEM coupling framework, solid motion is resolved at the particle-scale level (i.e., all the particles are tracked individually). The motion of each particle is governed by Newton's second law and the governing equations are expressed as

$$m_p \frac{d\boldsymbol{v}_p}{dt} = m_p \mathbf{g} - V_p \nabla p_g + \mathbf{f}_d + \mathbf{f}_c \tag{6}$$

$$I_p \frac{d\boldsymbol{\omega}_p}{dt} = \mathbf{T}_p \tag{7}$$

where $\boldsymbol{v}_p$, $\boldsymbol{\omega}_p$, m_p, I_p are the translational velocity, angular velocity, mass and moment of inertia of a particle, respectively. Further, $\mathbf{T}_p$ stands for the torque exerted on particle by other colliding particles and walls. The last three terms on the right-hand side of Eq. 6 stand for the far field pressure force, the drag force, and the contact force with other particles and walls, respectively. The drag force $\mathbf{f}_d$ is computed as follows

$$\mathbf{f}_d = \frac{V_p \beta}{\varepsilon_p} \left(\mathbf{u} - \boldsymbol{v}_p \right) \tag{8}$$

where $\varepsilon_p (= 1 - \varepsilon_g)$ is the solid concentration in the cell. β is calculated using a drag relation proposed by Koch and Hill[38] based on Lattice Boltzmann simulations

$$\beta_{\text{Koch\&Hill}} = \frac{18 \mu \varepsilon_g \varepsilon_p}{d_p^2} \left(F_0(\varepsilon_p) + \frac{1}{2} F_3(\varepsilon_p) \text{Re}_p \right) \tag{9}$$

where Re_p is the particle Reynolds number given by

$$Re_p = \frac{\varepsilon_g \rho_g |\mathbf{u} - \boldsymbol{v}_p| d_p}{\mu} \tag{10}$$

The functions F_0 and F_3 in Eq. 8 are computed as follows

$$F_0(\varepsilon_p) = \begin{cases} \dfrac{1 + 3\sqrt{\dfrac{\varepsilon_p}{2}} + \dfrac{135}{64}\varepsilon_p \ln(\varepsilon_p) + 16.14\varepsilon_p}{1 + 0.681\varepsilon_p - 8.48\varepsilon_p^2 + 8.16\varepsilon_p^3} & \text{if } \varepsilon_p < 0.4 \\ \dfrac{10\varepsilon_p}{\varepsilon_g^3} & \text{if } \varepsilon_p \geq 0.4 \end{cases} \tag{11}$$

$$F_3(\varepsilon_p) = 0.0673 + 0.212\varepsilon_p + \frac{0.0232}{\varepsilon_g^5} \tag{12}$$

Because the system evaluated is dense, the interaction between neighboring particles is frequent, hence giving rise to the collision-dominated flow behavior for solid motion. Thus, the contact between the colliding particles should be accounted for. In this work, the contact forces between the colliding particles are modeled using the spring-dashpot model initially proposed by Cundall and Strack.[39] Fundamentally, the contact force exerts on particle i by particle j has the normal and tangential components

$$\mathbf{f}_{cij} = \mathbf{f}_{cnij} + \mathbf{f}_{ctij} \tag{13}$$

where $\mathbf{f}_{cnij}$ and $\mathbf{f}_{ctij}$ are both decomposed into the spring force and the dashpot force as follows

$$\mathbf{f}_{cnij} = \mathbf{f}_{cnij}^{\text{S}} + \mathbf{f}_{cnij}^{\text{D}} = (-k_n \delta_{nij} - \eta_n \boldsymbol{v}_{nij} \cdot \boldsymbol{n}_{ij}) \boldsymbol{n}_{ij} \tag{14}$$

$$\mathbf{f}_{ctij} = \mathbf{f}_{ctij}^{\text{S}} + \mathbf{f}_{ctij}^{\text{D}} = \min\left(-k_t \delta_{tij} \boldsymbol{t}_{ij} - \eta_t (\boldsymbol{v}_{tij} \cdot \boldsymbol{t}_{ij}) \boldsymbol{t}_{ij}, \mu_p |\mathbf{f}_{cnij}| \boldsymbol{t}_{ij} \right) \tag{15}$$

where k_n and η_n stand for the spring and damping coefficients, respectively, in the normal direction; k_t and η_t represent the spring and damping coefficients, respectively, in the tangential direction; δ_{nij} and δ_{tij} represent the normal and tangential displacements, respectively, between the particle pair. Furthermore, $\boldsymbol{v}_{nij}$ and $\boldsymbol{v}_{tij}$ are the normal and tangential components of the relative velocity between the colliding particles, respectively; $\boldsymbol{n}$ and $\boldsymbol{t}$ are the unit vectors in the normal and tangential directions, respectively; the superscripts S and D stand for the spring and damping components, respectively; the subscripts t and n represent the variable components in the tangential direction and normal direction of a collision, respectively. In addition, μ_p stands for the friction coefficient between the colliding particles.

Computational Setup

Computational conditions

The geometry of the vessel used in the experiments by Chen[16] is adopted in the present study, as shown in Figure 1a. The upper part of the bed has a cross section of 300 mm × 100 mm (width × depth), while the total height is 1000 mm. The bottom of the setup consists of two similar chambers, with two parallel slots with a cross section of 4 mm × 30 mm each in the middle of each base, and diverging walls inclined at 60° to each base. In some test cases, a vertical partition plate is introduced into the bed to investigate the resulting effects on improving the spouting stability in the system operation. Specifically, the partition plate with a height of 300 mm is mounted in the upper part of the column, with the lower end of the plate at 250 mm above the bottom of the setup.

In this work, a total number of 2,590,000 spherical glass beads with particle diameter of 1.33 mm and particle density of 2490 kg/m^3 are randomly dispersed in the bed, then allowed to fall under the influence of gravity to form an initial packed bed with a height of 200 mm. Detailed physical and numerical parameters are summarized in Table 1, while a vertical planar view of the numerical grids of the spouted bed at $z/Z = 0.5$, z is the depth position evaluated and Z is the total depth of the setup, is presented in Figure 1b. The grids are nonuniform in sizes ranging from 3 to 7.5 mm, which is about 2.25–5.26 times larger than the particle diameter. The minimum grid size is applied in the X (i.e., width) direction while the maximum size is applied in the Y (i.e., height) direction at the upper part of the setup. Along the depth direction, a uniform grid with each sized at 5 mm is adopted. All simulations were carried out on a computational grid system consisting of 97 × 192 × 20 cells (width × height × depth). As the DEM approach is used for tracking the solid phase, the time step for solid motion should be small enough to mimic the interaction of colliding particles; the criterion suggested by Tsuji et al.[40] is adopted in this work. Different values of time step for gas and solid motions are adopted to achieve a stable simulation.[40] Specifically, in all the cases, the CFD time step was set as 1×10^{-4} s while the DEM time step as 2×10^{-6} s. Details related to the parameters and numerical settings of the current effort can be found in the previous work.[31,32]

When the concentration distributions of particles were very nonuniform along a certain direction, most of the particles would assemble at certain parts of the domain. This phenomenon is very common in the spouted bed. Thus, the nonuniform decomposition strategy for parallel computations was developed and coupled into the codes for improving the loading balance of CPUs in the parallel simulations. In the current simulation, the spouted bed was partitioned into two regions

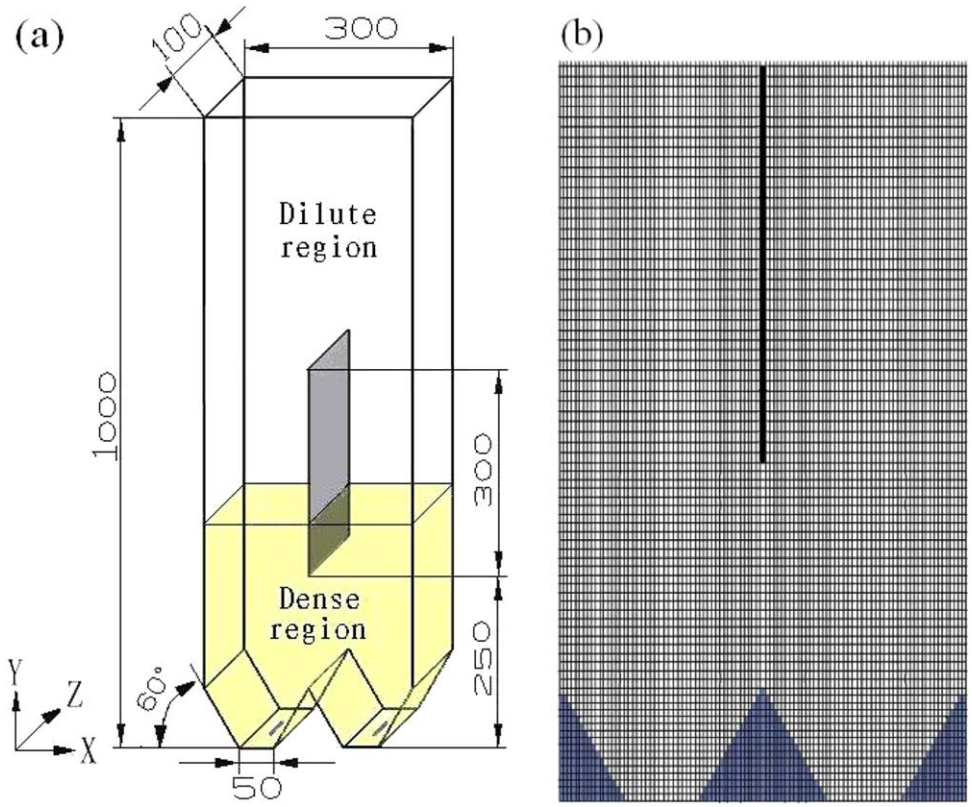

Figure 1. (a) Geometry of the computational domain, with the numbers representing the dimensions of the vessel in unit of mm; and (b) grid distribution in the central plane of $z/Z = 0.5$, where z is the depth position evaluated and Z is the total depth of the setup.

[Color figure can be viewed in the online issue, which is available at wileyonlinelibrary.com.]

in the Y direction, corresponding to the dense region at the lower part of the bed and the dilute region at the upper part of the bed. Moreover, in the present study, a total number of 112 CPUs in a cluster were used in the simulations, with more than two-thirds of the CPUs used for calculating the gas-solid hydrodynamics in the dense region that occupies three-tenth the height of the column. In previous work, a study of grid independence study has been carried out.[31]

Model verification

The numerical simulation was carried out on the open-source platform MFIX, which has been adopted for CFD-DEM studies of many fluidizing apparatus for both with and without chemical reaction.[41–43] For the current system, in order to verify the correctness of adopted numerical parameters, the pressure drop in the single slot-rectangular chamber with three different bed heights has been tested and the corresponding minimum spouting velocity has been compared with the experimental data.[30] Furthermore, the pressure drop profile with respect to decreasing spouting velocity in the double slot-rectangular spouted beds has been tested and also compared with the experimental data in the previous work. Based on the pressure drop profiles, two values of the minimum spouting velocities corresponding to the collapse of the two spouts in the two chambers were obtained, with less than 5% discrepancy with the experimental data. Besides, the fluctuation of

Table 1. Details of Physical Parameters Used in the Simulation

Parameters of gas phase			
Temperature (K)	298	Pressure (Pa)	1.013×10^5
Superficial gas velocity (m/s)	1.0–0.2	Viscosity (Pa s)	1.8×10^{-5}
Molecular weight (g/mol)	28.8	Density (kg/m^3)	1.205
Parameters of glass particles			
Number	2.59×10^6	Density (kg/m^3)	2490
Diameter (m)	1.33×10^{-3}	Spring constant (N/m)	800
Interparticle restitution coefficient	0.97	Interparticle friction coefficient	0.3
Particle-wall restitution coefficient	0.97	Particle-wall friction coefficient	0.25
Parameters related to the geometry of the 3-D setup			
Width (m)	0.3	Height (m)	1.0
Depth (m)	0.1	Slot width (m)	0.004
Slot depth (m)	0.03	Cells in X direction	97
Cells in Y direction	192	Cells in Z direction	20
Plate height (m)	0.3		

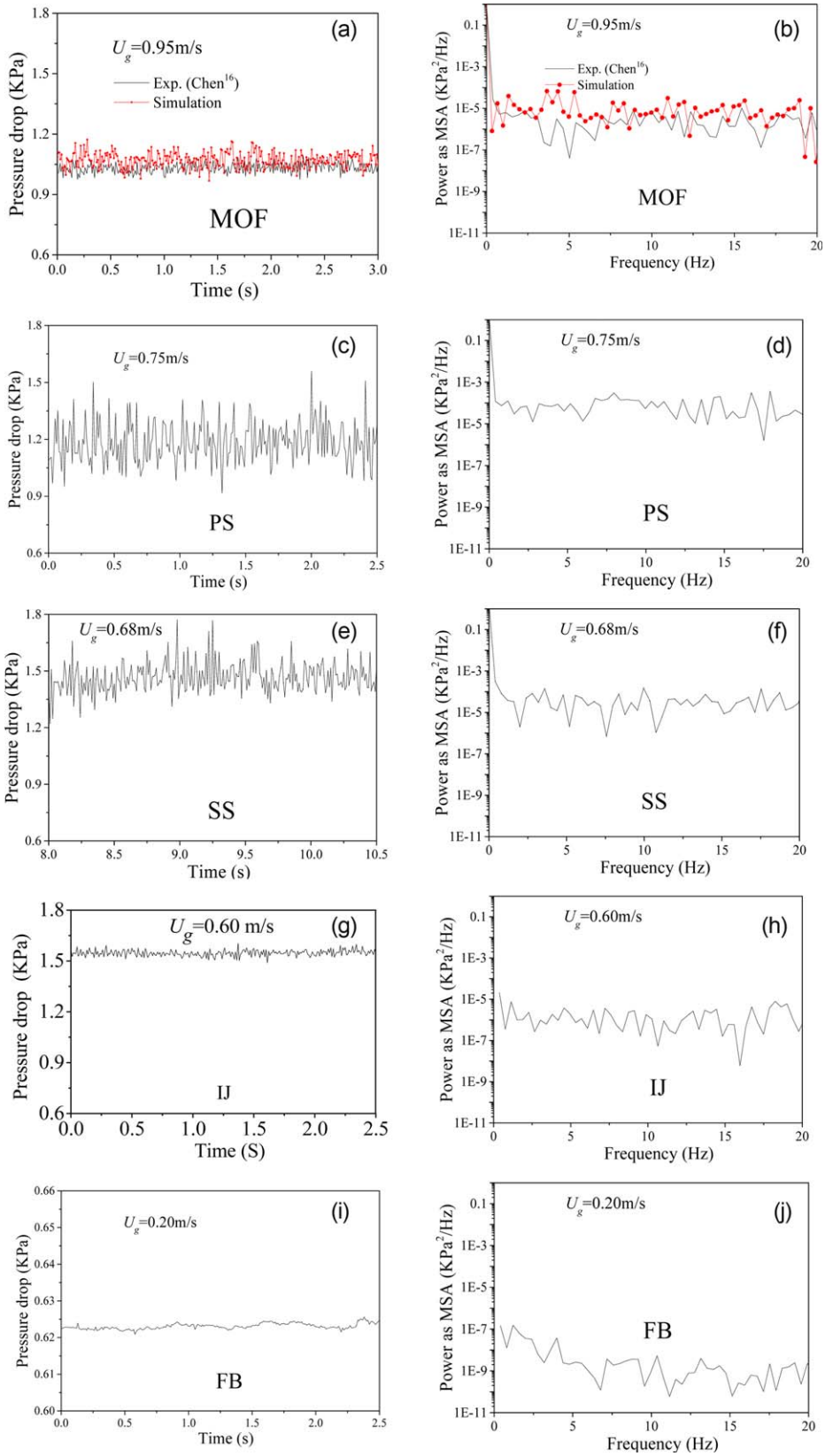

Figure 2. Profiles of pressure drop in the system operating in different flow regimes[31]: (a) MOF regime at $U_g = 0.9$ m/s; (c) PS regime at $U_g = 0.75$ m/s; (e) SS regime at $U_g = 0.68$ m/s (this regime appears when the spouting velocity is decreased from 0.69 to 0.68 m/s; the pressure drop is extracted after the system stabilizes at $t = 8.0$–10.5 s); (g) IJ regime at $U_g = 0.6$ m/s; and (i) FB regime at $U_g = 0.2$ m/s. Power spectra of the pressure fluctuations: (b) MOF regime at $U_g = 0.9$ m/s; (d) PS regime at $U_g = 0.75$ m/s; (f) SS regime at $U_g = 0.68$ m/s; (h) IJ regime at $U_g = 0.6$ m/s; and (j) FB regime at $U_g = 0.2$ m/s.

[Color figure can be viewed in the online issue, which is available at wileyonlinelibrary.com.]

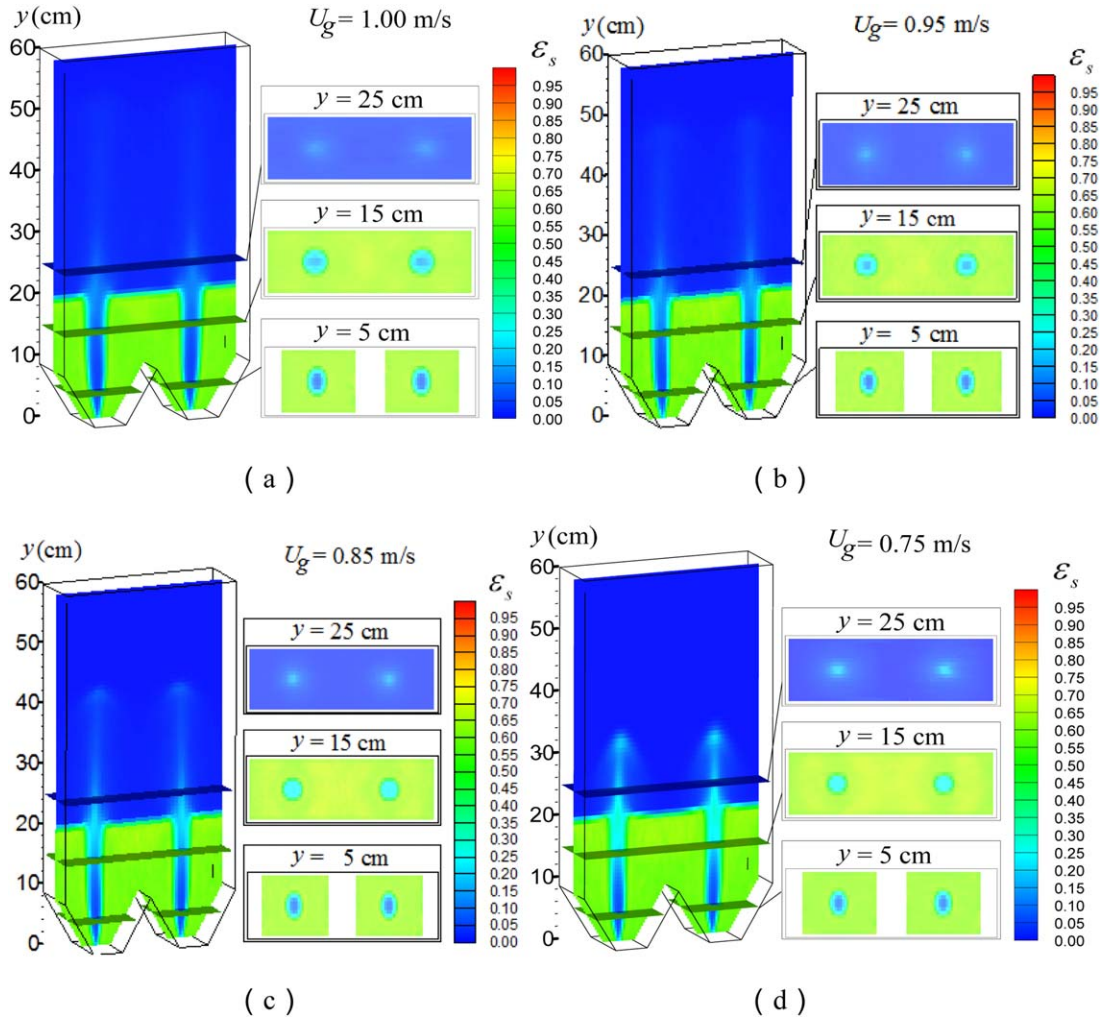

Figure 3. Contour plots of solid concentration at $z/Z = 0.5$ for a bed with an overall solid volume fraction of 0.3 for different spouting velocities (U_g), namely, (a) $U_g = 1.00$ m/s; (b) $U_g = 0.95$ m/s; (c) $U_g = 0.85$ m/s; and (d) $U_g = 0.75$ m/s.

[Color figure can be viewed in the online issue, which is available at wileyonlinelibrary.com.]

pressure drop and its power spectra of mean square amplitude (MSA) extracted in this apparatus shows agreement with the experimental data, indicating the simulation with adopted parameters can adequately address the important characteristics in the fluidizing process.

Results and Discussions

Fluctuations and power spectra of pressure signals in multiple-spouted bed

The gas-solid flow patterns in the multiple-spouted bed experience five distinct flow regimes depending on the gas supply through the gas inlet, as has been reported previously[16,31]: (1) merging of fountain (MOF), which is a merging of two fountains although the two spouts are still vertical and distinct; (2) parallel spouting (PS), whereby the two fountains are separate from each other; (3) single spouting (SS), whereby one of the spouts collapses to be an internal jet, while the other slot still exhibits steady spouting behavior. Significant interactions between the two spouts are found during the collapse, which is a focus of this work; (4) internal jets (IJ), whereby further decrease of the gas flow rate leads to the vanishing of the second fountain; and (5) fixed bed (FB), whereby, for very low gas velocity, caves or jets that formed at the two slots disappears.

On top of the macroscopic change of the gas-solid flow behavior, pressure drop signals in terms of the average value, fluctuations, and power spectra contain important information about the regimes. Takens[44] showed that the time series of the local pressure in a fluidized bed could reconstruct the dynamic state of the system. Pressure fluctuations were used by Freitas et al.[45] to identify the flow regimes in slot-rectangular spouted beds. In this work, the pressure drop between the inlet and outlet of the left chamber (Figure 1) was obtained, and spectral analyses of the pressure fluctuations were carried out. As shown in Figure 2, the pressure fluctuations and the associated power, expressed as mean square amplitude (MSA), evolve with different gas velocities (U_g), which correspond to different regimes. It should be mentioned that the SS regime appears when decreasing the spouting velocity from 0.69 to 0.68 m/s. More in-depth analyses can be found in the following section. Thus, the pressure drop is extracted when the system stabilizes after the adjustment, specifically at $t = 8.0$–10.5 s. Specifically, while Figures 2a, c, e, g, i present the simulated pressure

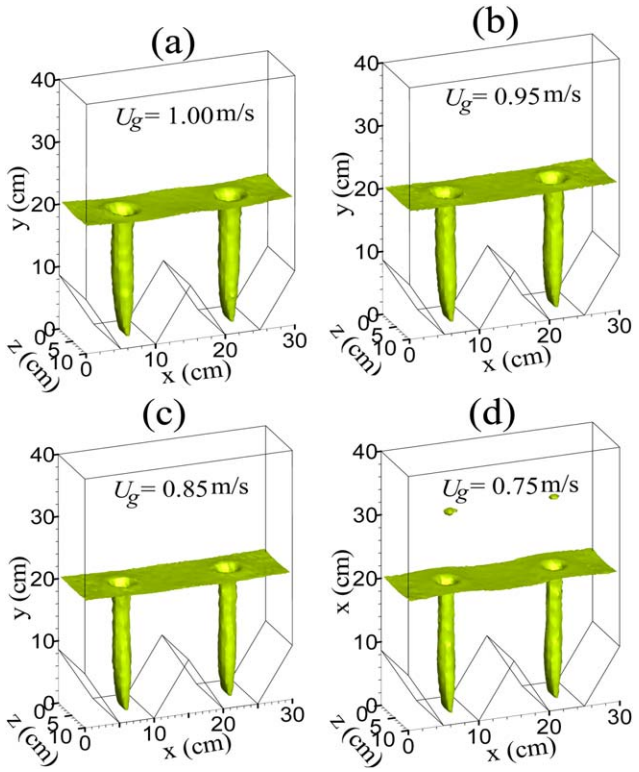

Figure 4. Plots of the simulated iso-surface for a bed with an overall solid volume fraction of 0.3 at different gas velocities (U_g), namely, (a) $U_g = 1.00$ m/s; (b) $U_g = 0.95$ m/s; (c) $U_g = 0.85$ m/s; and (d) $U_g = 0.75$ m/s.

[Color figure can be viewed in the online issue, which is available at wileyonlinelibrary.com.]

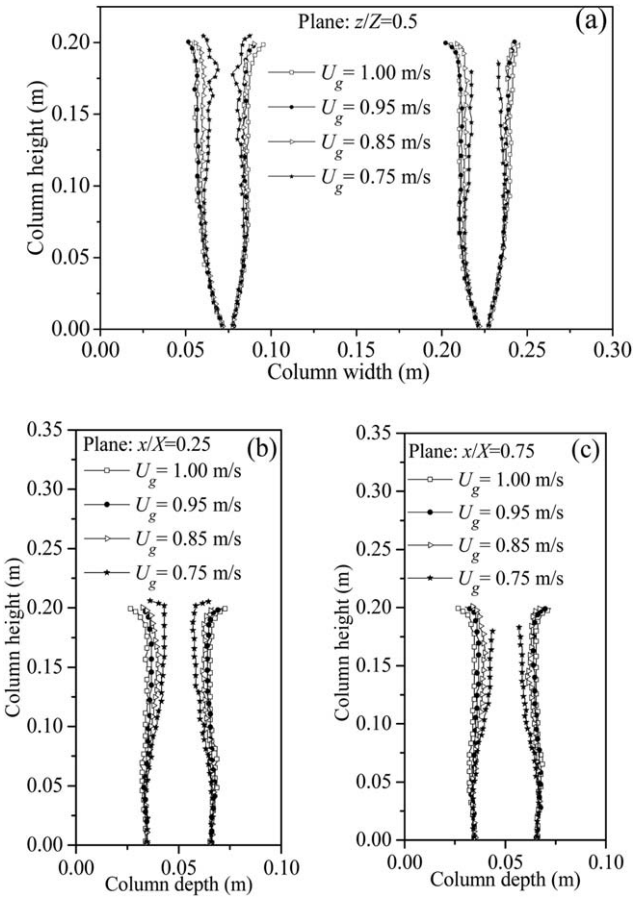

Figure 5. Spout shapes and sizes in the bed: (a) *xy* plane at $z/Z = 0.5$; (b) *yz* plane at $x/X = 0.25$, where *x* is the width position evaluated and *X* is the total width of the setup; and (c) *yz* plane at $x/X = 0.75$.

drops with time for different five regimes, Figures 2b, d, f, h, j present the corresponding trends of MSA.

Notably, the simulated pressure drop signals have been validated by experiments: for the MOF regime, Figure 2a shows that the simulated pressure fluctuations have slightly higher magnitudes than the experimental data, while Figure 2b shows better agreement of the power spectra curves between simulation and experiment. In general, Figure 2 shows that as U_g decreases from 0.95 to 0.20 m/s, both the magnitude of the pressure and extent of fluctuations increases then decreases (Figures 2a, c, e, g, i), while the magnitude of MSA in the power spectra analysis correspondingly also display the same nonmonotonic behavior in that the MSA increases then decreases. Further regarding the power spectra, all curves contain no significant peak and the magnitudes of the power are low, which means that the particles flux and the gas flux are continuous and steady in the regimes investigated.

The nonmonotonic behavior of the pressure signal with U_g warrants a closer look. Specifically, as U_g decreases from 0.95 to 0.75 m/s (i.e., MOF to PS regime transition), both the magnitudes of the pressure and extent of fluctuation (Figures 2a, c), and also magnitude of MSA (Figures 2b, d) increased, which is mainly due to the shrinkage of spout diameters and the increment of particle number densities in the spout regions. Because gas flow resistances along the two spouts increase and the pressure fluctuations induced by the particle motions become more dominant, higher pressure values and fluctuations appeared, as shown in Figure 2c. As U_g continues to decrease from 0.75 to 0.60 m/s (i.e., the regime transition from PS to SS and then to IJ), the magnitude of the pressure drop increases but extent of fluctuations decreases (especially Figure 2g), which corresponds to smoother fluidization. When U_g is at 0.20 m/s, the system is operated as a FB, which corresponds to the minimal fluidization expected in fluidized beds, hence both the magnitude of the pressure drop and extent of fluctuations are low. As such systems are typically operated in steady spouting conditions, the focus of this work is on the MOF and PS regimes. Furthermore, because the collapse of one of the spouts has important implications for system stability, the detailed study of the mechanisms leading to the collapse has also been carried out.

Solid concentration

In the spouting apparatus, particles are transported upward in the spout region, then ejected into the fountain region, followed by a slower downward trajectory in the annulus region. The significantly different behaviors in these three regions lead to three distinctive distributions of solid concentration. Figure 3 illustrates the 3-D distribution of solid concentration in the double slot-rectangular spouted bed operated at various spouting velocities (U_g). When U_g is high at 1.00 m/s (Figure 3a), the solid concentration in the spout region and fountain region is low. With the decrease of U_g, the solid concentration in these two regions increases gradually (Figures 3b–d). When U_g is low at 0.75 m/s (Figure 3d), the high solid concentration in the spout region restricts the maximum height of the spout,

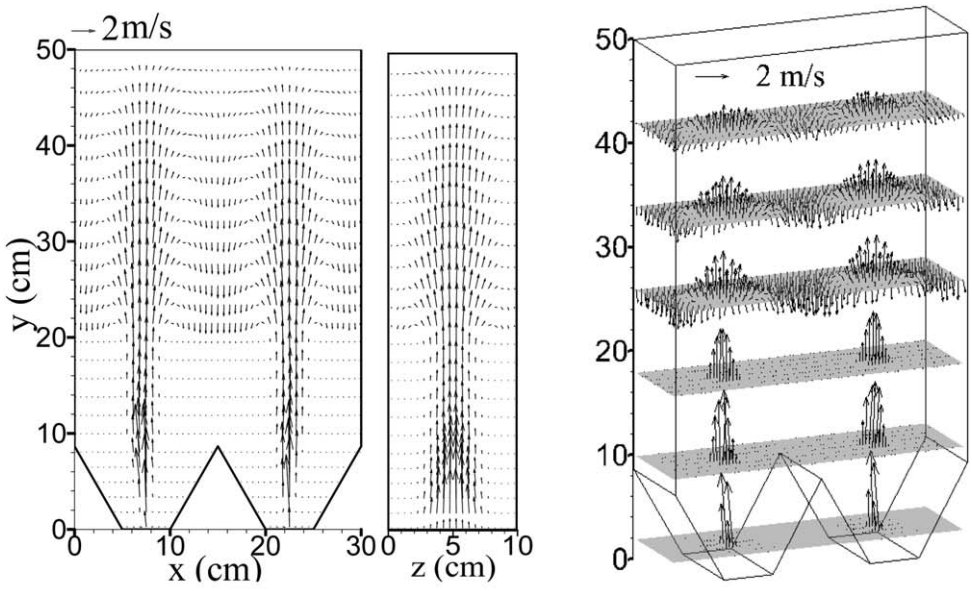

(a) $U_g = 0.95$ m/s

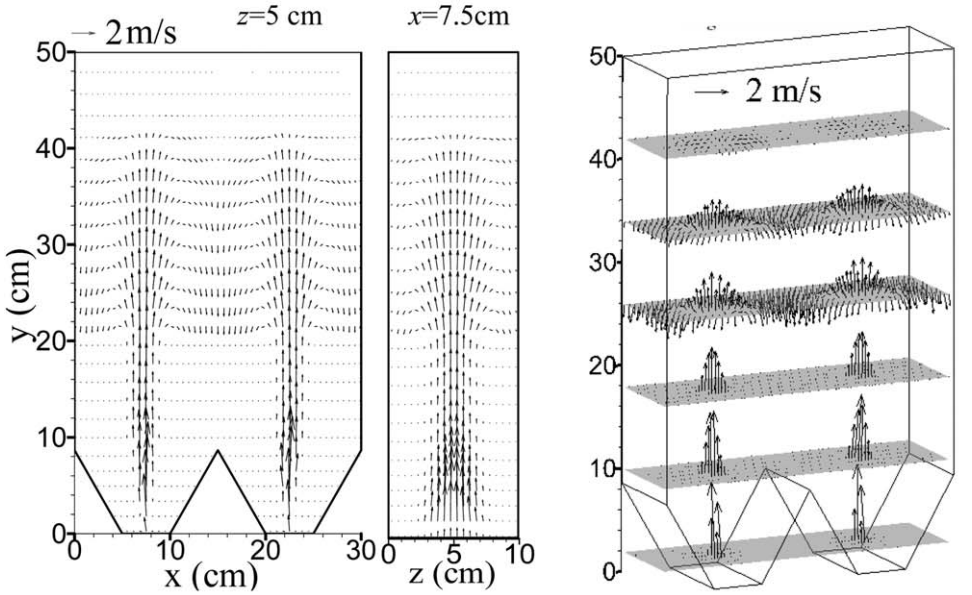

(b) $U_g = 0.85$ m/s

Figure 6. Vector field of the time-averaged particle velocity for the *xy* plane at $z/Z = 0.5$, for the *yz* plane at $x/X = 0.75$, and the 3-D view at various U_g values: (a) $U_g = 0.95$ m/s; (b) $U_g = 0.85$ m/s; and (c) $U_g = 0.75$ m/s.

which may have implications on the stable operation of the multiple spouted bed. Furthermore, the cross-sectional shape of the gas channel is observed to be similar to the spout inlet, namely the slot geometry, lower in the bed (i.e., $y = 5$ cm), then tends to be more circular higher in the bed (i.e., $y \geq 15$ cm).

Spout shapes and spout sizes

In the spouted bed, the existence of three distinct regions (i.e., spout, annulus, and fountain) with significantly different gas-solid flow behavior is well-acknowledged. As has been rigorously illustrated in a previous work,[31] the particles in the annulus region of the double slot-rectangular spouted bed enter the spout region through the spout-annulus interface along the bed height. Investigation on the unique spout-annulus interaction of the double slot-rectangular spouted bed is useful for understanding the dynamics between these two regions and also extremely helpful for the design and insertion of internal draft tubes to enhance operational stability in some cases. In this apparatus, stable and steady spouts are observed in the multiple-spouted bed in the regimes investigated of MOF and PS. A series of the simulated iso-surfaces for a bed with an overall solid volume fraction of 0.3 at various superficial gas velocities (U_g) are presented in Figure 4, which shows that all spouts in the range of U_g considered of 0.75–1.00 m/s have similar shapes and positions. The cross-section of each

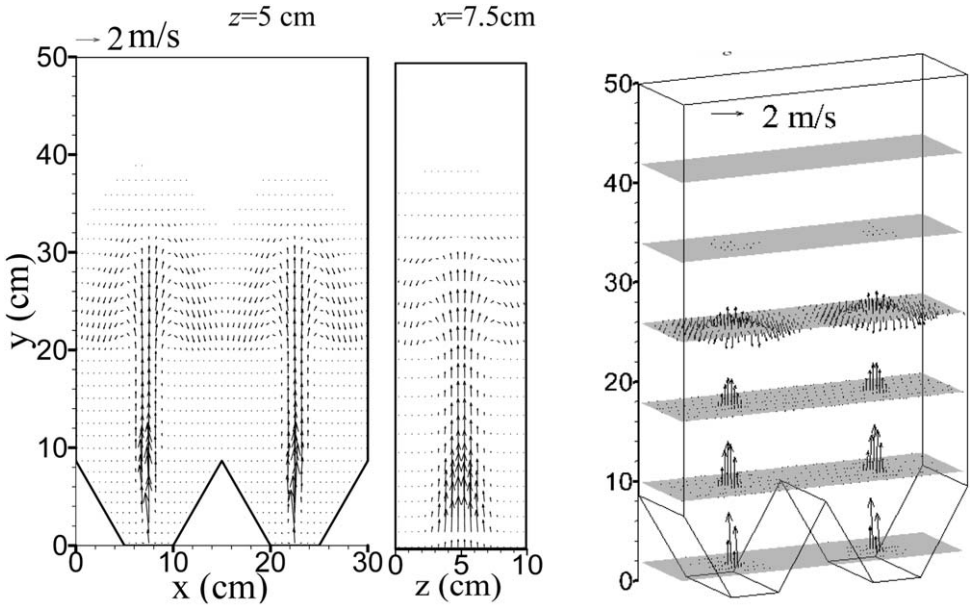

(c) $U_g = 0.75$ m/s

Figure 6. (Continued).

spout is rectangular in shape near the slot, then gradually becomes circular midway through the bed. Two types of spout shapes,[5] namely, "expanding, necking, and expanding" and "continuously diverging," are observed in this study, as illustrated in the detailed sizes of spouts summarized in Figure 5. The first type of spout shape (i.e., expanding, necking, and expanding) appears along both the *xy* plane and *yz* plane at the lower U_g values, but transforms to the second type (i.e., continuously diverging) at the higher U_g values. In addition, the cross-sectional diameter of the spout decreases as U_g decreases. The trends of spout shapes and sizes are similar to the experimental results obtained for a single-slot-spouted bed investigated by Chen.[16]

Vector fields of time-averaged particle flows

The vector fields of the time-averaged particle velocity are effective for showcasing detailed information about the dynamics of such systems. In Figure 6, a series of planar views of the vector fields of the time-averaged particle velocity are displayed. Generally, faster moving particles are observed in the spout and fountain regions, while slower moving particles are observed in the annular region. Particles in each chamber are carried upward by gas along the spout channel to the fountain region, then scattered to the surroundings, followed by downward movement in the annular region. The particle motion in the two orthogonal planes (i.e., *xy* and *yz* planes) display very different vector fields of time-averaged particle velocity. In the *xy* plane, the spout enlarges gradually with height. However, in the *yz* plane, the spout increases in size initially before shrinking, followed by enlargement again, which is in consistent with the variation of the spout boundary described in Figure 5.

The influence of spouting velocity (U_g) on the vertical motion of the solid phase at different heights is quantitatively compared in Figure 7. As U_g decreases, the height of the spout decreases (Figure 7a) and the tendency for the separate spouts from the two chambers to merge diminishes (Figure 7b), which in turn diminishes the tendency for the fountains to merge (Figure 7c). The impact of varying U_g is most apparent in the fountain region (Figure 7c), whereby the highest U_g of 0.95 m/s displays negative velocities in the annulus and regions between the two chambers, whereas the lowest U_g of 0.75 m/s displays approximately positive velocities in these regions.

Interactions between chambers during the collapse of one of the two spouts

From the investigations on the pressure drop of the two chambers and also the flow pattern in the earlier section on 'Fluctuations and power spectra of pressure signals in multiple spouted bed', it is known that, as U_g decreases, the spouting extent in the two chambers decreases in one chamber first before the other, instead of in parallel. Notably, although the initial packing status of the solid phase is similar in the two chambers in this work, the minimum spouting velocity appears to be different in each chamber, which is mainly due to the highly nonlinear behavior of the gas-solid motion in this system. In particular, the determination of the minimum spouting velocity of a spouting apparatus is by decreasing the total gas flow rate until the transition from the stable flow regime to the FB regime is observed. In the case of a double slot-rectangular spouted bed, the minimum spouting velocities are different in the two chambers, because the distribution of gas flow to the two chambers is different due to the different spouting extents. In this section, we attempt to reveal the intrinsic mechanisms of the mutual interactions between the two spouts when one of them collapses. At time $t = t_0$, the superficial gas velocity (U_g) is decreased from 0.69 to 0.68 m/s (Figure 8a), following which we get a series of snapshots with respect to time of the particle distributions and the gas velocity distributions of the *xy* plane at $z/Z = 0.5$, as shown in Figure 8, to explore the complex variations of gas-solid flow in this process.

Because 0.68 m/s is less than the minimum spouting velocity of the left chamber, the fountain heights of the two chambers start to decrease, with the height declining more for the

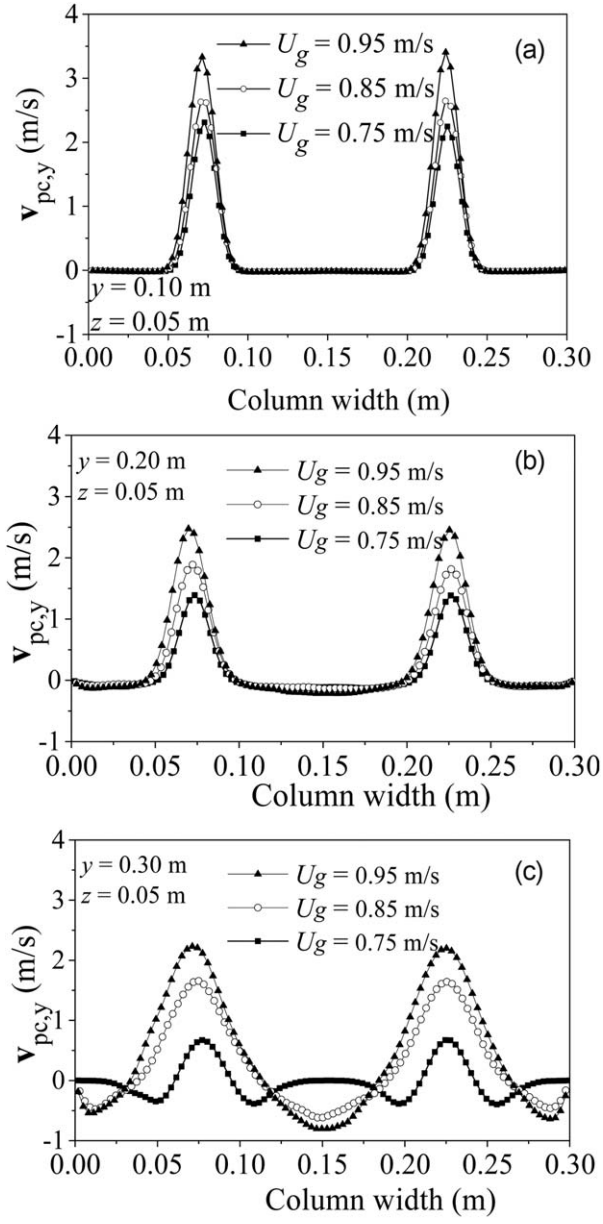

Figure 7. Time-averaged particle velocity on the *xy*-plane at *z*/*Z* = 0.5 at heights of (a) *y* = 0.10 m, (b) *y* = 0.20 m, and (c) *y* = 0.30 m.

left than the right chamber (Figure 8b). Particularly for the left chamber, as the gas flow is unable to sustain spouting, the fountain disappears and the spout region becomes blocked, thereby giving rise to the phenomenon of spouting collapse. Further on Figure 8c at $t = t_0 + 3.1$ s, the fountain disappears for the left chamber, while the fountain height of the right decreases slightly more. Figures 8d, e show that the spout height in the left chamber remains low (i.e., corresponding to the IJ regime), while the fountain height on the right chamber starts to increase to beyond the initial height at $t = t_0$ (Figure 8a).

Inspection of the corresponding distributions of vertical gas velocity (U_{g2}) reveals more on this behavior. As the spout in the left chamber collapses, U_{g2} in the left chamber decreases, which is mainly because the gas channel is restricted by the high concentration of particles in this region. The restriction to the gas flow in the left chamber exacerbates as more and more particles accumulate near the spout exit of this chamber, resulting in a greater consumption of gas momentum. This dynamic process lasts until the momentum decrease of rising gas counteracts the energy needed to penetrate the particles above. As the gas channel is unrestricted in the right chamber with the steady spouting behavior, more gas preferentially travels upward in the less-resistant right chamber.

With respect to the horizontal gas velocity (U_{g1}) component, the blocking of the gas channel in the left chamber changes the gas interaction between the two chambers. Initially, U_{g1} appears to be similar in the two chambers; however, this symmetry is disrupted with the collapse of the spout in the left chamber. The change of the distribution of U_{g1} occurs both in the region below the bed surface and the free board region above the surface. For the region beneath the bed surface, the area of positive U_{g1} is enlarged, while that of negative U_{g1} is reduced, which indicates the increase in the horizontal component of gas velocity corresponds with the decrease in the vertical one. Notably, this shift demonstrates that part of the rising gas introduced from the inlet of left chamber leaks into the right chamber, hence giving rise to the increase of gas flow below the bed surface for the right chamber, eventually resulting in the fountain height of the right chamber increasing beyond the initial height. After the rising gas ejects into the fountain region where the solid concentration is low, the interaction between the chambers is self-regulated to attain a new balance, which is the steady spouting of the solid phase in the right chamber with a slight incline to the left chamber.

In summary, the sudden collapse of the spout in the left chamber leads to a transitional behavior for a few seconds. After the self-adjustment, a new stable operation is achieved in the bed. The collapse of the spout in the left chamber seems to benefit that in the right chamber, for the height of the right fountain decreases at first before increasing to a height even greater than the initial fountain height.

Effects of the partition plate

In the multiple-spouted bed, the interaction between adjacent spouts may lead to the termination of some spouts and thereby instability of system operation. Experiments carried by Chen[16] revealed that the merging of the fountains is the main form of interactions between two spouts. Accordingly, a vertical partition can be introduced to prevent the interactions between adjacent fountains. The bed hydrodynamics of a double slot-rectangular spouted bed with a partition plate has been studied in the previous work,[32] along with the effect of the installation height of the partition plate in the fountain region.

In this work, case studies with and without vertical partitions (geometry shown in Figure 1a) in the flow regime of MOF were investigated. The snapshots of the flow patterns at two different superficial gas velocities (U_g) are presented in Figure 9. Qualitatively, the fountain heights in the partitioned column appear similar to that without partition. However, the quantitative comparison of time-averaged solid vertical velocity indicated that the solid velocity and concentration in the spout-annulus region are only slightly affected by the partition plate, but more vigorous motion of the solid phase can be observed in the central region and the near-wall region of the fountain in each chamber due to the increased pressure drop in the presence of a partition plate.[32] However, the mechanism underlying the role of the partition plate in improving the

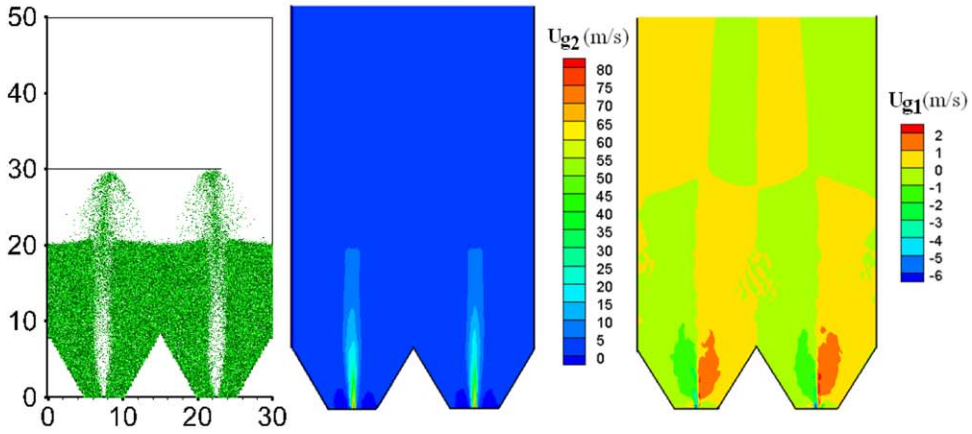

(a) t=t_0 s

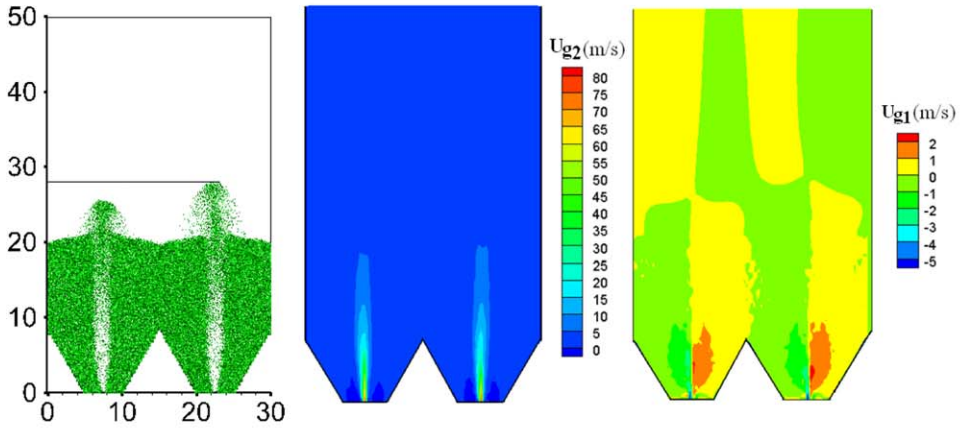

(b) t=t_0+2.0 s

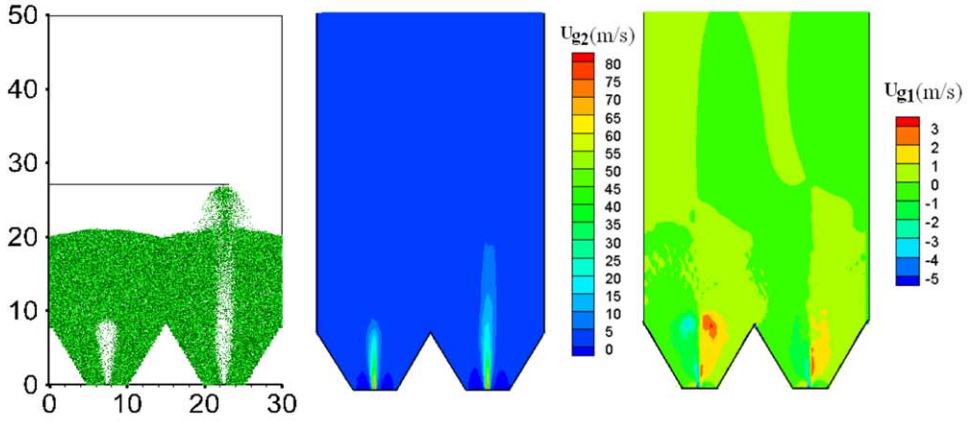

(c) t=t_0+3.1 s

Figure 8. Solid flow behavior and contour plots of vertical gas velocity (U_{g2}) and horizontal gas velocity (U_{g1}) gas velocity at $z/Z = 0.5$ when one of the spouts collapses at time steps of: (a) $t = t_0$ s; (b) $t = t_0 + 2.0$ s; (c) $t = t_0 + 3.1$ s; (d) $t = t_0 + 3.6$ s; (e) $t = t_0 + 4.6$ s.

[Color figure can be viewed in the online issue, which is available at wileyonlinelibrary.com.]

operational stability in multiple-spout systems has not been presented before.

Figure 10 shows the contour plots of the instantaneous vertical (U_{g2}) and horizontal (U_{g1}) components of the gas velocity at the time beyond which the system stabilizes after the adjustment of U_g, in the double slot-rectangular spouted bed with or without a partition plate in the central plane of $z/Z = 0.5$. With respect to the vertical component of the gas velocity, except for the region with the partition plate, where slower gas velocities are apparent near the surface of the plate (Figure 10c), the

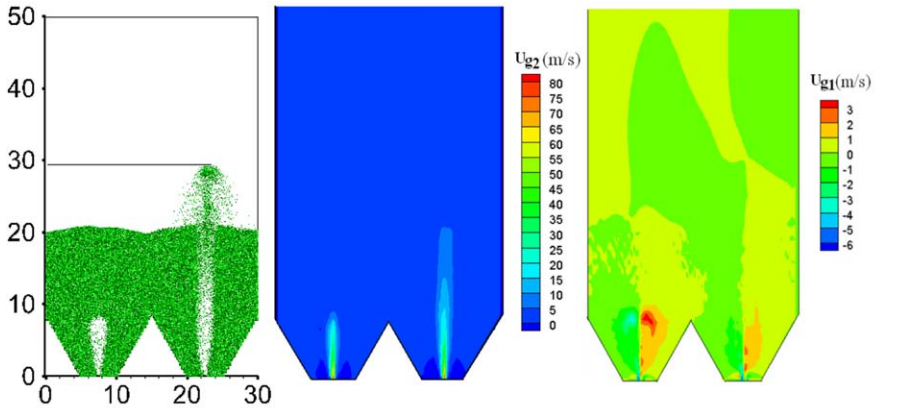

(d) t=t_0+3.6 s

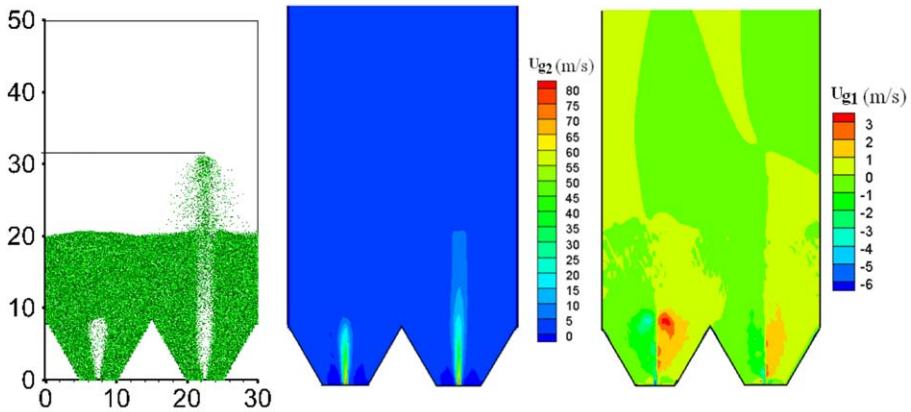

(e) t=t_0+4.6 s

Figure 8. (Continued).

[Color figure can be viewed in the online issue, which is available at wileyonlinelibrary.com.]

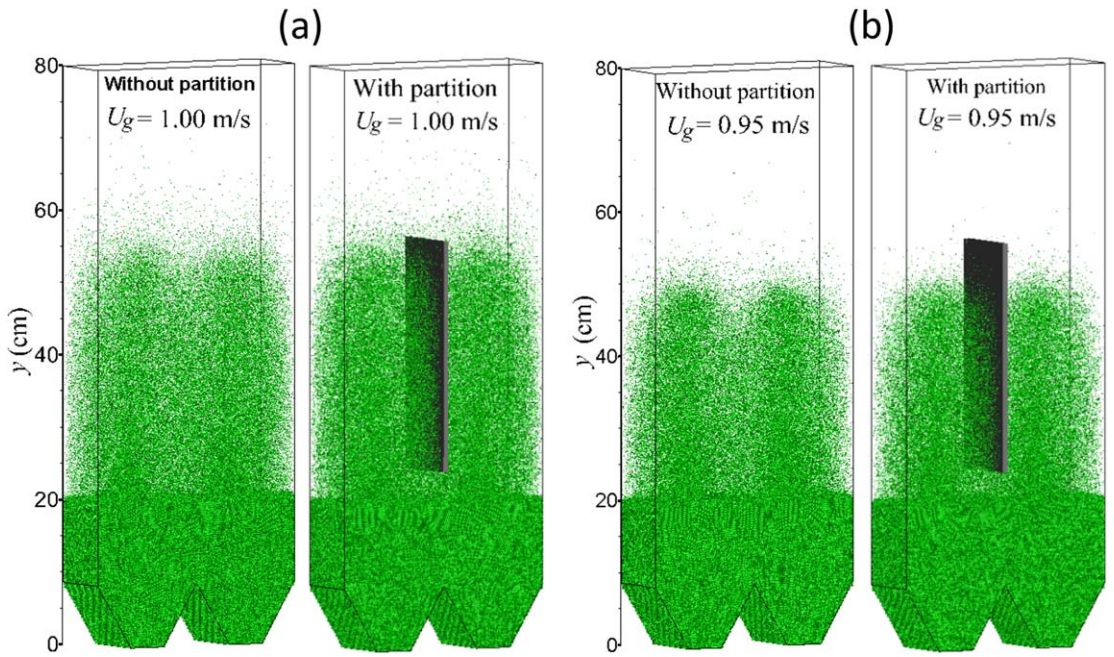

Figure 9. Comparison of the solid motion in the multiple-spouted bed with and without a vertical partition at (a) U_g = 1.0 m/s and (b) U_g = 0.95 m/s.

[Color figure can be viewed in the online issue, which is available at wileyonlinelibrary.com.]

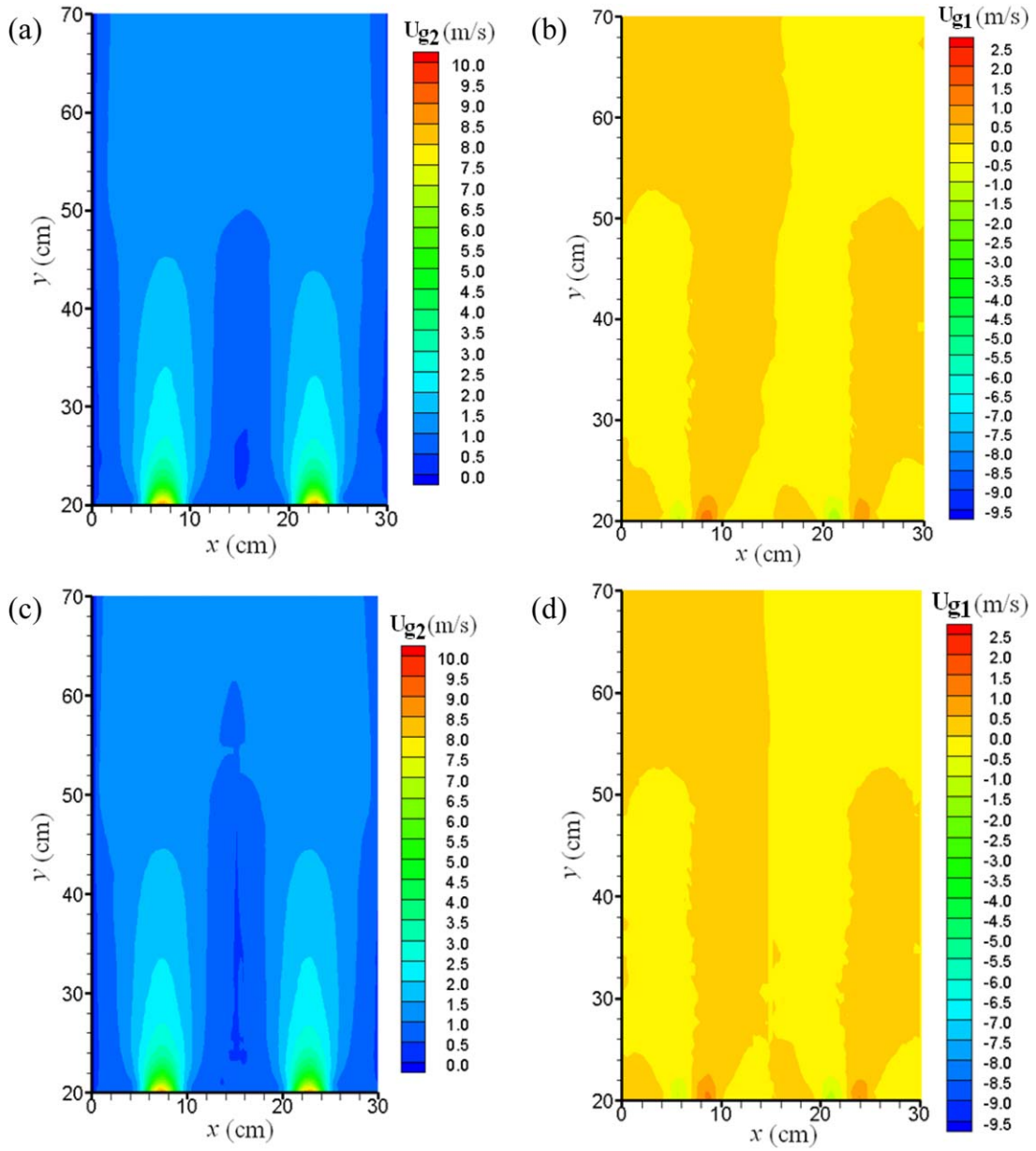

Figure 10. Contour plots of the instantaneous gas velocity along the vertical (U_{g2}) and horizontal (U_{g1}) directions in the central plane of $z/Z = 0.5$ of the multiple-spouted bed: (a) vertical gas velocity (U_{g2}) without the vertical partition, (b) horizontal gas velocity (U_{g1}) without the vertical partition, (c) vertical gas velocity (U_{g2}) with the vertical partition, and (d) horizontal gas velocity (U_{g1}) with the vertical partition.

[Color figure can be viewed in the online issue, which is available at wileyonlinelibrary.com.]

general distribution of U_{g2} is similar whether in the presence or absence of the partition plate. As for the horizontal component of the gas velocity (Figures 10b, d), the presence of partition plate blocks the gas interchange and mutual interaction of these two chambers in the fountain region, resulting in a more stable flow of gas in each chamber, which allows for operational stability.

In view of the observation that the partition plate inserted above the bed surface reduces the gas interaction between these two chambers and hence circumvents the SS phenomenon, it would be interesting to seek an optimized design of such an internal insertion to prevent the potential instability in the system operation. These investigations are part of an ongoing effort.

Conclusions

The parallel CFD-DEM simulations have been successfully validated against experimental results, and then used to further predict the gas-solid hydrodynamics in a multiple-spouted bed. Based on the simulation, four objectives have been accomplished: (1) the pressure drop of different flow regime has been analyzed; (2) the spout shape and solid concentration in the bed has been probed; (3) the intrinsic mechanisms of interchamber interaction leading to the collapse of a spout has been studied; and (4) the effect of inserting a vertical particle plate has been explored. Some useful conclusions can be drawn from this study as listed below:

1. The average of the pressure drop and corresponding fluctuations differ according to the gas velocities in different

flow regimes. The maximum spouting height decreases as the spouting velocity decreases.

2. Two shapes of spouts are identified along the X and Z directions, and spout sizes decrease with decreasing gas velocity. Detailed information about the dynamics of the multiple-spouted bed is revealed by the vector fields of the time-averaged particle velocity.

3. Rigorous gas-solid interaction between two chambers occurs when one of the spouts collapses due in part to the aggregation of particles at the upper part of the spout. The collapsing of one spout seems to benefit the other spout, for the height of the remaining fountain height decreases at first and then increases to a height even greater than the initial fountain height.

4. Operational instability due to spout collapse can be averted by placing a vertical partition to separate neighboring spouts and fountains in a multiple-spouted bed. The partition plate is expected to be particularly beneficial in ensuring operational stability when scaling up such systems.

To harness the benefits of spouted bed technology in industrial-scale operations, more understanding is still needed especially of multiple-spouted bed. Further studies on the interactions between chambers for systems with three or more chambers, setups with different bases or various particle numbers, and heat-transfer characteristics would be useful.

Acknowledgments

The authors are grateful for the help of Dr. Tingwen Li on the parallel code of MFIX-DEM. S.L.Y and J.W.C would like to thank for the Financial support from the National Research Foundation (NRF), Prime Minister's Office, Singapore under its Campus for Research Excellence and Technological Enterprise (CREATE) program.

Notation

d_p = particle diameter, m
$\mathbf{f}_c$ = contact force, N
$\mathbf{f}_{cnij}$ = normal contact force, N
$\mathbf{f}_{ctij}$ = tangential contact force, N
$\mathbf{f}_d$ = drag force, N
$\mathbf{f}_p$ = far field pressure force, N
$\mathbf{g}$ = gravitational acceleration, m/s^2
I = particle moment of inertia, kg m^2
k = turbulent kinetic energy, m^2/s^2
k_n = spring coefficient in normal direction, N/m
k_t = spring coefficient in tangential direction, N/m
m_p = particle mass, kg
$\boldsymbol{n}$ = normal unit vector between colliding pair, dimensionless
p_g = pressure, Pa
Re_p = particle Reynolds number, dimensionless
t = time instant, s
$\boldsymbol{t}$ = tangential unit vector of colliding pair, dimensionless
$\mathbf{T}_p$ = particle torque, N m
$\mathbf{u}$ = gas velocity vector, m/s
U_g = superficial gas velocity, m/s
U_{g1} = horizontal gas velocity, m/s
U_{g2} = vertical gas velocity, m/s
$\mathbf{V}_{\mathrm{pc,y}}$ = particle vertical velocity, m/s
V_{cell} = volume of current computational cell, m^3
V_p = particle volume, m^3
V_{pi} = volume of particle i in a cell, m^3

Greek symbols

β = interphase momentum transfer coefficient, kg/(m^{3}s)
δ_{nij} = normal displacement between particle i and particle j, m
δ_{tij} = tangential displacement between particle i and particle j, m
ε_g = void fraction, dimensionless
ε_p = solid concentration, dimensionless
ε_t = turbulent dissipation rate, m^2/s^3
μ = gas dynamic viscosity, kg/(m s)
μ_p = friction coefficient between colliding particle-particle or particle-wall pair, dimensionless
μ_t = gas turbulence viscosity, kg/(m s)
$\boldsymbol{v}_p$ = particle velocity, m/s
ρ_g = gas density, kg/m^3
$\boldsymbol{\omega_p}$ = particle angular velocity, s^{-1}
η_n = damping coefficient in normal direction, kg/s
η_t = damping coefficient in tangential direction, kg/s

Subscripts

c = contact force
d = drag force
g = gas phase
p = particle phase
t = turbulence

Abbreviations

CFD = computational fluid dynamics
DEM = discrete element method
FB = fixed bed
IJ = internal jets
MOF = merging of fountain
MSA = mean square amplitude
PS = parallel spouting
SS = single spouting
2-D = two-dimensional
3-D = three-dimensional

Literature Cited

1. Mathur KB, Gishler PE. A technique for contacting gases with coarse solid particles. *AIChE J*. 1955;1:157–164.
2. Olazar M, Aguado R, Bilbao J, Barona A. Pyrolysis of sawdust in a conical spouted-bed reactor with a HZSM-5 catalyst. *AIChE J*. 2000; 46:1025–1033.
3. Benkrid A, Caram HS. Solid flow in the annular region of a spouted bed. *AIChE J*. 1989;35:1328–1336.
4. Bahramian A, Olazar M. Fluidization of micronic particles in a conical fluidized bed: experimental and numerical study of static bed height effect. *AIChE J*. 2012;58:730–744.
5. Mathur KB, Epstein N. Developments in spouted bed technology. *Can J Chem Eng*. 1974;52:129–144.
6. Stocker RK, Eng JH, Svrcek WY, Behie LA. Ultrapyrolysis of propane in a spouted-bed reactor with a draft tube. *AIChE J*. 1989;35: 1617–1624.
7. Feng H, Tang J, Cavalieri RP, Plumb OA. Heat and mass transport in microwave drying of porous materials in a spouted bed. *AIChE J*. 2001;47:1499–1512.
8. Albina DO. Emissions from multiple-spouted and spout-fluid fluidized beds using rice husks as fuel. *Renew Energy*. 2006;31:2152–2163.
9. Hu G, Gong X, Wei B, Li Y. Flow patterns and transitions of a novel annular spouted bed with multiple air nozzles. *Ind Eng Chem Res*. 2008;47:9759–9766.
10. Murthy DVR, Singh PN. Minimum spouting velocity in multiple spouted beds. *Can J Chem Eng*. 1994;72:235–239.
11. Saidutta MB, Murthy DVR. Mixing behaviour of solids in multiple spouted beds. *Can J Chem Eng*. 2000;78:382–385.
12. Ren B, Zhong W, Zhang Y, Jin B, Wang X, Tao H, Xiao R. Investigation on flow patterns and transitions in a multiple-spouted bed. *Energy Fuel*. 2010;24:1941–1947.
13. Mujumdar A. *Spouted bed technology – a brief review. Drying*. New York: Hemisphere-McGraw-Hill, 1984.
14. Dogan OM, Freitas LAP, Lim CJ, Grace JR, Luo B. Hydrodynamics and stability of slot-rectangular spouted beds. Part I: thin bed. *Chem Eng Commun*. 2000;181:225–242.
15. Freitas L, Dogan OM, Lim CJ, Grace JR, Luo B. Hydrodynamics and stability of slot-rectangular spouted beds part II: increasing bed thickness. *Chem Eng Commun*. 2000;181:243–258.
16. Chen Z. *Hydrodynamics, Stability and Scale-Up of Slot-Rectangular Spouted Beds*. Vancouver: University of British Columbia, 2008.

17. van Buijtenen MS, van Dijk W, Deen NG, Kuipers JAM, Leadbeater T, Parker DJ. Numerical and experimental study on multiple-spout fluidized beds. *Chem Eng Sci*. 2011;66:2368–2376.
18. Deen NG, Van Sint Annaland M, Van der Hoef MA, Kuipers JAM. Review of discrete particle modeling of fluidized beds. *Chem Eng Sci*. 2007;62:28–44.
19. Hoef Van Der MA, Sint Annaland Van M, Deen NG, Kuipers JAM. Numerical simulation of dense gas-solid fluidized beds: a multiscale modeling strategy. *Annu Rev Fluid Mech*. 2008;40:47–70.
20. Yang S, Luo K, Fan J, Cen K. Particle-scale investigation of the solid dispersion and residence properties in a 3-D spout-fluid bed. *AIChE J*. 2014;60:2788–2804.
21. Fang M, Luo K, Yang S, Zhang K, Fan J. Computational fluid dynamics-discrete element method investigation of solid mixing characteristics in an internally circulating fluidized bed. *Ind Eng Chem Res*. 2013;52:7556–7568.
22. Yang S, Luo K, Fang M, Fan J, Cen K. Discrete element study of solid circulating and resident behaviors in an internally circulating fluidized bed. *Chem Eng J*. 2014;248:145–157.
23. He Y, Deen NG, van Annaland MS, Kuipers JAM. Gas−solid turbulent flow in a circulating fluidized bed riser: numerical study of binary particle systems. *Ind Eng Chem Res*. 2009;48:8098–8108.
24. Kawaguchi T, Sakamoto M, Tanaka T, Tsuji Y. Quasi-three-dimensional numerical simulation of spouted beds in cylinder. *Powder Technol*. 2000;109:3–12.
25. Link JM, Deen NG, Kuipers J, Fan X, Ingram A, Parker DJ, Wood J, Seville J. PEPT and discrete particle simulation study of spout-fluid bed regimes. *AIChE J*. 2008;54:1189–1202.
26. Link JM, Cuypers LA, Deen NG, Kuipers JAM. Flow regimes in a spout–fluid bed: a combined experimental and simulation study. *Chem Eng Sci*. 2005;60:3425–3442.
27. Swasdisevi T, Tanthapanichakoon W, Charinpanitkul T, Kawaguchi T, Tanaka T, Tsuji Y. Investigation of fluid and coarse-particle dynamics in a two-dimensional spouted bed. *Chem Eng Technol*. 2004;27:971–981.
28. Takeuchi S, Wang S, Rhodes M. Discrete element method simulation of three-dimensional conical-base spouted beds. *Powder Technol*. 2008;184:141–150.
29. Zhong W, Xiong Y, Yuan Z, Zhang M. DEM simulation of gas–solid flow behaviors in spout-fluid bed. *Chem Eng Sci*. 2006;61:1571–1584.
30. Yang S, Luo K, Fang M, Zhang K, Fan J. Three-dimensional modeling of gas–solid motion in a slot-rectangular spouted bed with the parallel framework of the computational fluid dynamics–discrete element method coupling approach. *Ind Eng Chem Res*. 2013;52:13222–13231.
31. Yang S, Luo K, Zhang K, Qiu K, Fan J. Numerical study of a lab-scale double slot-rectangular spouted bed with the parallel CFD–DEM coupling approach. *Powder Technol*. 2015;272:85–99.
32. Yang S, Luo K, Fang M, Zhang K, Fan J. Parallel CFD–DEM modeling of the hydrodynamics in a lab-scale double slot-rectangular spouted bed with a partition plate. *Chem Eng J*. 2014;236:158–170.
33. Li T, Garg R, Galvin J, Pannala S. Open-source MFIX-DEM software for gas-solids flows: part II—validation studies. *Powder Technol*. 2012;220:138–150.
34. Garg R, Galvin J, Li T, Pannala S. Open-source MFIX-DEM software for gas–solids flows: part I—verification studies. *Powder Technol*. 2012;220:122–137.
35. Li T, Gopalakrishnan P, Garg R, Shahnam M. CFD–DEM study of effect of bed thickness for bubbling fluidized beds. *Particuology*. 2012;10:532–541.
36. Zhao XL, Li SQ, Liu GQ, Yao Q, Marshall JS. DEM simulation of the particle dynamics in two-dimensional spouted beds. *Powder Technol*. 2008;184:205–213.
37. Ren B, Zhong W, Jin B, Yuan Z, Lu Y. Computational fluid dynamics (CFD)–discrete element method (DEM) simulation of gas–solid turbulent flow in a cylindrical spouted bed with a conical base. *Energy Fuel*. 2011;25:4095–4105.
38. Koch DL, Hill RJ. Inertial effects in suspension and porous-media flows. *Annu Rev Fluid Mech*. 2001;33:619–647.
39. Cundall PA, Strack ODL. A discrete numerical model for granular assemblies. *Geotechnique*. 1979;9:47–65.
40. Tsuji Y, Kawaguchi T, Tanaka T. Discrete particle simulation of two-dimensional fluidized bed. *Powder Technol*. 1993;77:79–87.
41. Breault RW, Guenther C. Mass transfer coefficient prediction method for CFD modeling of riser reactors. *Powder Technol*. 2010; 203:33–39.
42. Hosseini SH, Ahmadi G, Rahimi R, Zivdar M, Esfahany MN. CFD studies of solids hold-up distribution and circulation patterns in gas–solid fluidized beds. *Powder Technol*. 2010;200:202–215.
43. Pu W, Zhao C, Xiong Y, Liang C, Chen X, Lu P, Fan C. Numerical simulation on dense phase pneumatic conveying of pulverized coal in horizontal pipe at high pressure. *Chem Eng Sci*. 2010;65:2500–2512.
44. Takens F. *Detecting Strange Attractors in Turbulence*. Berlin: Springer, 1981.
45. Freitas LAP, Dogan OM, Lim CJ, Grace JR, Bai D. Identification of flow regimes in slot-rectangular spouted beds using pressure fluctuations. *Can J Chem Eng*. 2004;82:60–73.

Manuscript received Apr. 11, 2015, and revision received June 11, 2015.